



Research Paper

In situ construction of hierarchical $\text{WO}_3/\text{g-C}_3\text{N}_4$ composite hollow microspheres as a Z-scheme photocatalyst for the degradation of antibioticsTingting Xiao^a, Zheng Tang^a, Yong Yang^{a,b,*}, Lanqin Tang^{b,c}, Yong Zhou^{b,**}, Zhigang Zou^b^a Key Laboratory of Soft Chemistry and Functional Materials, Ministry of Education, Nanjing University of Science and Technology, Nanjing 210094, PR China^b Eco-Materials and Renewable Energy Research Centre (ERERC), Jiangsu Key Laboratory for Nano Technology, School of Physics, Nanjing University, Nanjing 210093, PR China^c College of Chemistry and Chemical Engineering, Yancheng Institute of Technology, Yancheng 224051, PR China

ARTICLE INFO

Keywords:

Antibiotic
Hollow microsphere
Tungsten oxide
 $\text{g-C}_3\text{N}_4$
Z-Scheme

ABSTRACT

Elegant Z-scheme $\text{WO}_3/\text{g-C}_3\text{N}_4$ composite hollow microspheres (CHMs) were constructed through precisely controlled in situ hydrolysis and a polymerization process consecutively. The formation of intact and well-defined hollow microspheres can be realized through optimizing the ratio of precursors for WO_3 and $\text{g-C}_3\text{N}_4$. The shell of these hollow microspheres consist of well-distributed WO_3 and $\text{g-C}_3\text{N}_4$ nanoparticles, and excellent heterojunctions with numerous interfaces and highly exposed oxidation-reduction active sites have thus been built. By virtue of this special architecture, more incident photons are expected to be trapped in the hollow cavities, which contribute to more electrons and holes available for photocatalytic reactions. Moreover, these photoinduced hole-electron pairs could be effectively separated, and the lifetime of charge carriers reaches 2.23 ns, which is obviously prolonged compared with the $\text{WO}_3/\text{g-C}_3\text{N}_4$ CHMs as an optimized Z-scheme system retains the original oxidation and reduction abilities for the components without change of the oxidation and reduction potential. Combined with the long survival time of holes and electrons, this photocatalyst showed enhanced degradation rates towards tetracycline hydrochloride (TC-HCl) and ceftiofur sodium (CFS).

1. Introduction

The discovery and utilization of antibiotics was a significant step forward for mankind, allowing us to contend with bacterial infections, which are regarded as the first threat to human health. Until recent years, the problem of the misuse of antibiotics has attracted scientific and public attentions. The phenomenon of antibiotic resistance has become more and more evident, and residues of antibiotics are found in a variety of environmental matrices, including surface and groundwater, soils, waste and even the food on our table [1,2]. The quantities of these pharmaceuticals presented only increase and never decrease, which directly threatens the life conditions of the whole ecosystem. The well-known controversy surrounding DDT helped to first put antibiotics disposal on the public agenda.

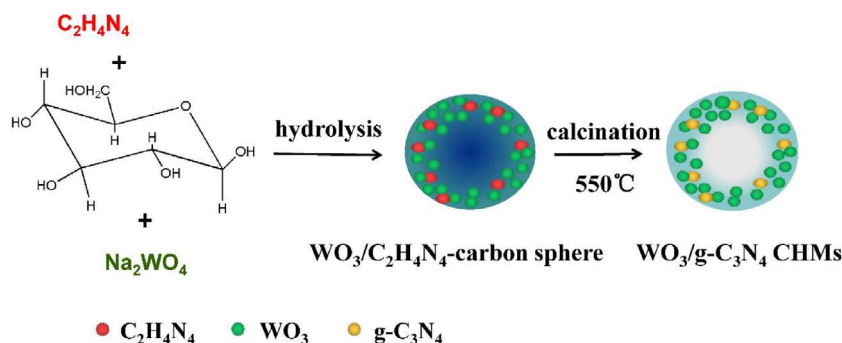
In the past few years, various technologies for environmental contaminant abatement have been used to treat the antibiotics, including physical adsorption [3–5], biological treatment [6,7] and chemical degradation [8]. The latter is regarded as an effective and thorough solution. Chemical methods oxidize the antibiotics to substances that

are easily biodegradable and less toxic, and even transform them into harmless compounds [9]. Among many advanced oxidation processes, photocatalysis has been described as one of the most promising due to its energy-savings, environmental friendliness and low cost [10,11]. Semiconductors illuminated by renewable solar energy that exceed the band gap energy produce amounts of electrons (e^-) and holes (h^+). The electrons and holes could react respectively with oxygen and hydroxyl ions (OH^-) adsorbed on the catalyst surface to generate hydrogen peroxide and hydroxyl radicals ($\cdot\text{OH}$), and they are strong oxidants for the degradation of organics. Metal oxides, including TiO_2 [12–14], ZnO [15–17], SnO_2 [18], WO_3 [19,20], and others have been widely investigated for the photodecomposition of pollutants with the aid of light irradiation. Among them, tungsten oxide (WO_3) shows excellent visible-light-driven photocatalytic activity due to its narrow band gap energy of approximately 2.7–2.8 eV [21]. As visible light occupies 45% of the entire solar spectrum, WO_3 has great potential for environmental remediation with low resource consumption. Moreover, the position of the valence band for WO_3 is relatively high, and the holes generated on WO_3 therefore have intense capability for oxidizing

* Corresponding author at: Key Laboratory of Soft Chemistry and Functional Materials, Ministry of Education, Nanjing University of Science and Technology, Nanjing 210094, PR China.

** Corresponding author.

E-mail addresses: yw6729@163.com (Y. Yang), zhouyong1999@nju.edu.cn (Y. Zhou).



OH^- into $\cdot\text{OH}$, which has been demonstrated to be a vital intermediate step in the process of photodecomposition. Due to the rapid recombination of photoinduced hole-electron pairs, however, there are few instances for the utilization of WO_3 in the treatment of antibiotics.

Many studies have devised heterostructured photocatalysts with diverse models for WO_3 [22] and $\text{g-C}_3\text{N}_4$ [23–25]. Based on the heterojunctions, the effective separation of charge carriers is realized, and the photocatalytic activity and stability of photocatalysts are improved. Cui et al. [26] prepared $\text{WO}_3/\text{g-C}_3\text{N}_4$ photocatalysts via a facile one-step simultaneously heating procedure using urea and tungsten chloride as the precursors. WO_3 particles with the size of 30–50 nm were covered on the $\text{g-C}_3\text{N}_4$ surfaces or embedded in $\text{g-C}_3\text{N}_4$ layers. These composites showed significant enhancement in photodegradation of Rhodamine B by virtue of the heterostructures. Tsubota's group [27] synthesized the composite of $\text{g-C}_3\text{N}_4$ and WO_3 using a planetary mill, and the prepared photocatalyst showed high photocatalytic activity for acetaldehyde decomposition under visible-light irradiation as a result of Z-scheme charge transfer. Katsumata et al. [28] used $\text{g-C}_3\text{N}_4$ nanosheets for the preparation of a $\text{g-C}_3\text{N}_4/\text{WO}_3$ composite in which WO_3 particles were covered on the surfaces of $\text{g-C}_3\text{N}_4$. The composite exhibited enhanced photocatalytic activity for the degradation of acetaldehyde. Despite these exciting advances in the field of photocatalysis for WO_3 , there are still problems regarding efficiency. The low utilization rate of photons and fewer surface active sites seriously restrict their practical applications [29]. Various morphologies of semiconductors are thus being designed, including nanosheets [30], nanorods [31], nanocubes [32], and others. Hollow structures have attracted intense attention for many years due to their special structural, physical and chemical properties [33–35]. This cavity structure endows the material with low density, high specific surface area, favourable efficiencies of mass transfer and utilization of photons. Our group has reported a variety of hollow spheres with different compositions for the photocatalytic reduction of CO_2 , including $\text{Ti}_{0.91}\text{O}_2/\text{CdS}$ hollow spheres with alternated multilayer structure [36], $\text{Au}@\text{TiO}_2$ yolk-shell hollow spheres with surface plasmon resonance effect [37], and GaN double-shelled hollow spheres with oxygen doping [38].

In this article, we demonstrate an in situ hydrolysis and polymerization process for the construction of $\text{WO}_3/\text{g-C}_3\text{N}_4$ composite hollow microspheres (CHMs). The formation of intact and well-defined hollow microspheres is realized when the ratio of the precursors for WO_3 and $\text{g-C}_3\text{N}_4$ is well optimized. The specific hollow structure allows the trapping of incident light for a long time, and provides high efficiency for photon utilization. Moreover, the shells of the microspheres are constructed by the well-distributed WO_3 and $\text{g-C}_3\text{N}_4$ nanoparticles. Numerous interfaces between WO_3 and $\text{g-C}_3\text{N}_4$ can thus be built, and the separation efficiency of photoinduced electron–hole pairs was improved. Compared with the WO_3 , $\text{WO}_3/\text{g-C}_3\text{N}_4$ CHMs possesses a longer charge carrier lifetime of 2.23 ns and highly exposed oxidation-reduction active sites, which obviously improve the oxidation and reduction abilities of the catalyst. The powerful heterojunctions as a Z-scheme system retains the original oxidation and reduction abilities for the components without changing their oxidation and reduction potential,

Scheme 1. Schematic representation of in situ construction of $\text{WO}_3/\text{g-C}_3\text{N}_4$ composite hollow microspheres (CHMs).

and the photodegradation rates towards tetracycline hydrochloride (TC-HCl) and ceftiofur sodium (CFS) are thus improved.

2. Experimental

2.1. Chemicals and materials

Sodium tungstate dihydrate (Aladdin, 99.5%) was used as a precursor for the preparation of WO_3 . Dicyandiamide (Aladdin, 99%) was used as a precursor for the preparation of $\text{g-C}_3\text{N}_4$. Ceftiofur sodium ($\text{C}_{19}\text{H}_{16}\text{N}_5\text{O}_7\text{S}_3\text{Na}$, CFS) and tetracycline hydrochloride ($\text{C}_{22}\text{H}_{24}\text{N}_2\text{O}_8\text{HCl}$, TC-HCl) obtained from Macklin were employed as the target organic pollutants. 5, 5-dimethyl-1-pyrroline-N-oxide (DMPO) purchased from Sigma-Aldrich was used as the trapping agent for investigation of $\cdot\text{OH}$ and $\cdot\text{O}_2^-$ radicals. Glucose was the product of Aladdin, and other chemicals used in the experiments were purchased from the Shanghai Chemical Reagent Company.

2.2. Preparation of $\text{WO}_3/\text{g-C}_3\text{N}_4$ composite hollow microspheres (CHMs)

As described in Scheme 1, $\text{WO}_3/\text{g-C}_3\text{N}_4$ CHMs were prepared using an in situ hydrolysis and polymerization process with a hydrothermal method combining calcination. In a typical procedure, 1 mmol Na_2WO_4 was added to 50 mL of deionized water while stirring to form a homogeneous solution. Subsequently, a certain amount of dicyandiamide and 25 mmol of glucose were introduced, and the resulting mixture was continuously stirred for 30 min. Afterwards, the homogeneous solution was transferred to a Teflon-lined stainless steel autoclave with a capacity of 100 mL. The autoclave was sealed and heated in an oven at 200°C for 20 h. After naturally cooling to room temperature, the solid products were subjected to centrifugation, washed with distilled water and ethanol three times, and finally dried in air at 60°C . In the next step, the as prepared dry products were annealed at 550°C for 3 h in air. According to the above manner, a series of $\text{WO}_3/\text{g-C}_3\text{N}_4$ composites with different contents of $\text{g-C}_3\text{N}_4$ were prepared and labelled $\text{WO}_3/\text{g-C}_3\text{N}_4\text{-x}$ for simplicity, where x represented the molar quantities of dicyandiamide added in the process of preparation.

WO_3 and $\text{g-C}_3\text{N}_4$ were prepared for comparison by using the same method. For the preparation of WO_3 , 1 mmol Na_2WO_4 and 25 mmol of glucose were added to 50 mL of deionized water to form a homogeneous solution under stirring. Then, the products were obtained by following the abovementioned steps. Meanwhile, to obtain $\text{g-C}_3\text{N}_4$, 5 g dicyandiamide was put into an alumina crucible that was heated at 550°C for 3 h with a temperature increase rate of 10 °C/min. After the reaction, the alumina crucible was cooled naturally to room temperature. The as-prepared $\text{g-C}_3\text{N}_4$ was collected and ground into powder for further use.

2.3. Catalyst characterization

The crystal structures were characterized using a Brucker-D8-Advanced X-ray diffraction equipped with Cu K α radiation source. The

FT-IR spectra were measured by a Nicolet IS10 infrared spectrometer. Morphologies of the samples were observed by field-emission scanning electron microscopy (FESEM, HITACHI S-4800) equipped with an energy-dispersive X-ray spectroscopy (EDS, Oxford instruments X-Max). Transmission electron microscopy (TEM) images were recorded by an FEI Tecnai F20 microscope at an accelerating voltage of 100 kV. X-ray photoelectron spectroscopy (XPS) was carried out on an RBD upgraded PHI-5000C ESCA system (Perkin-Elmer) with Mg K α radiation ($\hbar\nu = 1253.6$ eV). The binding energy of C1s (284.6 eV) was used to calibrate the other binding energies. The specific surface areas were measured using a JW-BK132F BET instrument and the pore diameter distribution was obtained from the absorption isotherms of N₂ using the Barrett-Joyner-Halenda (BJH) equation. UV-vis diffuse reflectance spectroscopy (UV-vis-DRS) was measured on a Shimadzu UV-2600 spectrometer. Photoluminescence (PL) emission spectra were recorded on a PerkinElmer LS 55 Fluorescence spectrometer at 355 nm. The fluorescence emission decay time data were obtained on a Horiba Jobin-Yvon Fluorolog-3-21-TCSPC spectrometer. The electron spin resonance (ESR) investigations were conducted with a Bruker EMX-10/12 ESR spectrometer. Magic angle spinning solid state nuclear magnetic resonance (NMR) spectrum was recorded using a Bruker Avance 400 MHz spectrometer with the spinrate of 10000 Hz, scan number of 40000 and referenced to the ¹³C chemical shift of TMS at 0 ppm.

2.4. Evaluation of photocatalytic activity

In the photocatalytic degradation of CFS and TC, the photochemical reactor was illuminated using a 300 W xenon lamp with a 420 nm cut-off filter. In each test, 50 mg of as-prepared samples were added into 100 mL of 25 mg/L antibiotics solution. Then, the suspension was stirred in the dark for 30 min to achieve the adsorption-desorption equilibrium before visible light irradiation. During irradiation, 5 mL of the suspension was taken out and centrifuged (10,000 rpm, 10 min) to remove the photocatalyst before measurement. The changes in concentration of CFS and TC-HCl were monitored by measuring the UV-vis absorption of the suspensions at 20 min interval. The peak absorbencies of CFS at 292 nm and TC at 357 nm were used to determine its concentration by a Shimadzu UV2600 spectrophotometer. The total organic carbon analyzer (elementar vario TOC, Germany) was applied to analyse the mineralization degree of antibiotics. To estimate the photostability of the photocatalysts, after one trial, the sample was collected through centrifugation, washed by deionized water and dried for the subsequent cycle test.

2.5. Evaluation of adsorption kinetics

The adsorption kinetics of the as-prepared samples were investigated by the adsorption experiments, which was carried out under the condition of continuous magnetic agitation at 25 °C. Typically, 100 mL of antibiotics aqueous solution (5 mg/L) was added to a 250 mL beaker, and 10 mg samples were added to the solution in dark. With continuous magnetic stirring, 5 mL of the suspension was removed and centrifuged (10,000 rpm, 10 min) to remove the photocatalyst before measurement. The concentration of the antibiotics was also measured by a Shimadzu UV2600 spectrophotometer.

2.6. Photo-electrochemical tests

Photo-electrochemical analysis was performed on a CHI660E electrochemical workstation in a standard three-electrode configuration with 0.5 M Na₂SO₄ solution as the electrolyte. The working electrode was prepared on the FTO glass. 5 mg of sample was dispersed in 1 mL of DMF by sonication to get a slurry mixture, after which the slurry was spin-coated onto the FTO. A Pt sheet was used as the counter electrode and saturated calomel electrode (SCE) as the reference electrode. Transient photocurrent and electrochemical impedance spectroscopy

(EIS) were carried out at the open circuit potential. A sinusoidal ac perturbation of 5 mV was applied to the electrode over the frequencies range from 0.01 to 10 KHz.

2.7. Active species trapping and ESR experiments

In the active species trapping experiments, 1 mM ethylenediaminetetraacetic acid (EDTA), 1 mM 1,4-benzoquinone (BQ) and 1 mM isopropanol (IPA) were respectively employed as the scavengers for h⁺, ·O₂⁻ and ·OH. Furthermore, presence of ·OH and ·O₂⁻ radicals was measured by the ESR technique using DMPO as the trapping agent. Before determining the ·OH and ·O₂⁻ radicals, 10.0 mg catalysts were dissolved in 0.5 mL deionized water or 0.5 mL methanol, and then 40 μL DMPO was added with ultrasonic dispersion for 5 min, respectively. The signals were collected after 5 min of irradiation under visible light.

3. Results and discussion

3.1. Structure and morphology

Fig. 1 shows the XRD patterns of WO₃, pristine g-C₃N₄ and WO₃/g-C₃N₄ composites. The diffractions for WO₃ are in good agreement with the standard monoclinic phase (JCPDS 83-0951). g-C₃N₄ shows two basic diffraction peaks at approximately 12.8° and 27.6°, reflecting the in-plane structural packing motif and inter-layer stacking of a conjugated aromatic system (JCPDS 87-1526), which can be well-indexed to (100) and (002) planes of graphitic materials [39]. All of the WO₃/g-C₃N₄ composites exhibit similar XRD patterns with that of the pure WO₃, which indicates WO₃ is the main component in the WO₃/g-C₃N₄ samples. No diffraction peaks corresponding to g-C₃N₄ are observed in the WO₃/g-C₃N₄-2 and WO₃/g-C₃N₄-4 composites, probably due to the low content of g-C₃N₄ in these samples. With the increase of g-C₃N₄ content, the intensities of diffraction peak at 27.6° in WO₃/g-C₃N₄-6 and WO₃/g-C₃N₄-8 becomes stronger and obvious, which demonstrates the presence of g-C₃N₄. Additionally, magic angle spinning solid-state NMR spectroscopy is used for investigation of WO₃/g-C₃N₄-8 (Fig. S1). The signals at 164.9 and 156.7 ppm are assigned to the sp²-hybridized carbon atoms of CN₂ (NH_x) and CN₃ in the g-C₃N₄ networks, respectively [40,41]. Moreover, FT-IR spectra (Fig. S2) exhibit similar results as the XRD, and the characteristic peaks of g-C₃N₄ could not be observed in the spectra of WO₃/g-C₃N₄-2, WO₃/g-C₃N₄-4 and WO₃/g-C₃N₄-6. For WO₃/g-C₃N₄-8, peaks attributable to the vibration of CN heterocycles can be clearly observed in the range of 1200–1650 cm⁻¹,

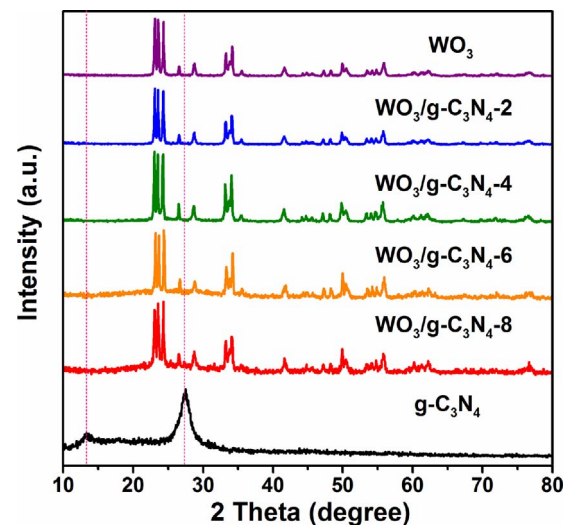


Fig. 1. XRD patterns of WO₃, g-C₃N₄ and WO₃/g-C₃N₄ composites.

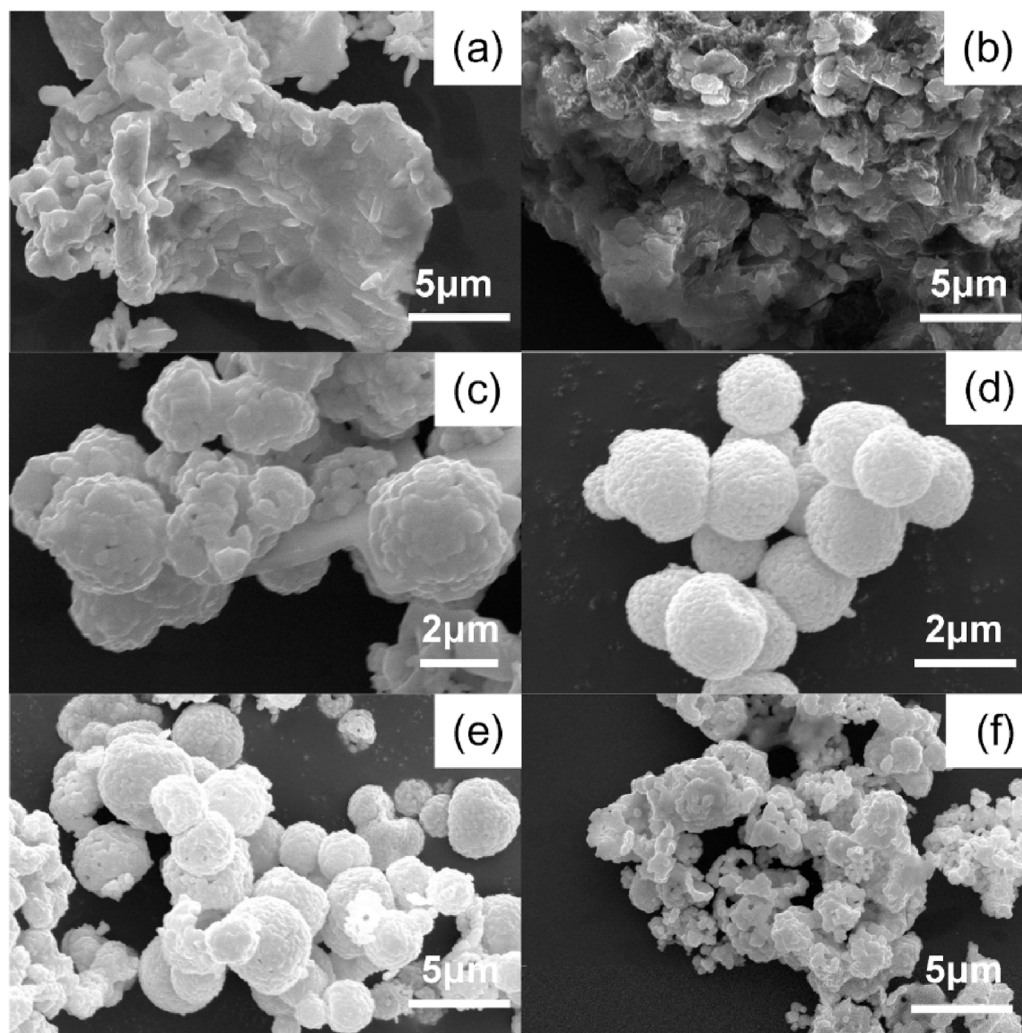


Fig. 2. FE-SEM images of (a) WO_3 , (b) $\text{g-C}_3\text{N}_4$, (c) $\text{WO}_3/\text{g-C}_3\text{N}_4\text{-}2$, (d) $\text{WO}_3/\text{g-C}_3\text{N}_4\text{-}4$, (e) $\text{WO}_3/\text{g-C}_3\text{N}_4\text{-}6$ and (f) $\text{WO}_3/\text{g-C}_3\text{N}_4\text{-}8$.

and the characteristic breathing mode of triazine units at approximately 810 cm^{-1} is also observed.

As displayed in Fig. 2a, WO_3 showed a bulky morphology composed of many irregular agglomerates. The synthesized $\text{g-C}_3\text{N}_4$ is constructed by the aggregation and gathering of the $\text{g-C}_3\text{N}_4$ nanosheets, and the structure seemed to be textured (Fig. 2b). The effect of the concentration of $\text{C}_2\text{H}_4\text{N}_4$ on the construction of $\text{WO}_3/\text{g-C}_3\text{N}_4$ composites was investigated in detail. Fig. 2c-2f show $\text{WO}_3/\text{g-C}_3\text{N}_4$ composites prepared by using different amounts of $\text{C}_2\text{H}_4\text{N}_4$ with a fixed value of Na_2WO_4 at 1 mmol. As shown, when the reaction was carried out with 2 mmol of $\text{C}_2\text{H}_4\text{N}_4$ ($\text{WO}_3/\text{g-C}_3\text{N}_4\text{-}2$), the composites are rough and irregular aggregates. There is little spherical structure. As the amount of $\text{C}_2\text{H}_4\text{N}_4$ increased to 4 mmol, the intact and well-defined microspheres were obtained, and their average diameters are arranged from 1.5 μm to 3 μm . When 6 mmol of $\text{C}_2\text{H}_4\text{N}_4$ was used, many microspheres were crushed and irregular aggregates of nanoparticles coexisted. In particular, no spheres were observed when 8 mmol of $\text{C}_2\text{H}_4\text{N}_4$ was attained. These observations indicated that the amount of $\text{C}_2\text{H}_4\text{N}_4$ played an important role in controlling the architecture of composites.

To demonstrate the interiors of these microspheres, special broken sites for $\text{WO}_3/\text{g-C}_3\text{N}_4\text{-}4$ composites were found. As shown in Fig. 3a and b, some cavities could be observed, which provides direct evidence for the hollow structure of these microspheres. It is worth noting that the hollow spheres are composed of many particulate $\text{g-C}_3\text{N}_4$ and WO_3 ; these nanoparticles assembled together and constructed a complete microsphere. This particular architecture would facilitate the formation of heterojunctions with numerous interfaces, which was a vital factor

for the improvement of photocatalysis. The structure of $\text{WO}_3/\text{g-C}_3\text{N}_4\text{-}4$ was further investigated by TEM. Although these microspheres are too thick to transmit the electron beam, the hollow interiors of the remaining microspheres can be identified by the contrast between the dark edges and the pale centres in Fig. 3c. As shown in Fig. 3d, the aggregated structure of the microspheres can be clearly observed. Crystalline WO_3 and $\text{g-C}_3\text{N}_4$ nanoparticles contributed to the formation of one microsphere, which is in accordance with the SEM analyses above.

The crystalline structure and elemental distributions of $\text{WO}_3/\text{g-C}_3\text{N}_4\text{-}4$ CHMs were further investigated by high resolution transmission electron microscopy (HRTEM) and elemental mappings. As shown in Fig. 4a, the lattice fringes with interlayer distances of 0.389 nm corresponding to the (002) lattice plane of WO_3 and 0.324 nm corresponding to the typical (002) interlayer-stacking of $\text{g-C}_3\text{N}_4$ can be indexed, which confirmed the composition of $\text{WO}_3/\text{g-C}_3\text{N}_4\text{-}4$ CHMs. The results are consistent with the XRD analyses. As shown in Fig. 4b, EDS elemental mapping images show the well distribution of the four elements of C, N, O and W, which demonstrates that both the WO_3 and $\text{g-C}_3\text{N}_4$ contribute to the formation of the hollow microspheres. Moreover, SEM elemental mappings (Fig. S3) also present the well distributions of these four elements of C, N, O and W.

Based on the above experimental results and investigations, we believe that the formation mechanism of the $\text{WO}_3/\text{g-C}_3\text{N}_4$ CHMs may be rationally interpreted as follows. At the beginning stage of reaction, the carbon spheres with hydrophilic surfaces are formed by the cross-linking between glucose [42]. Then, Na_2WO_4 and $\text{C}_2\text{H}_4\text{N}_4$ are

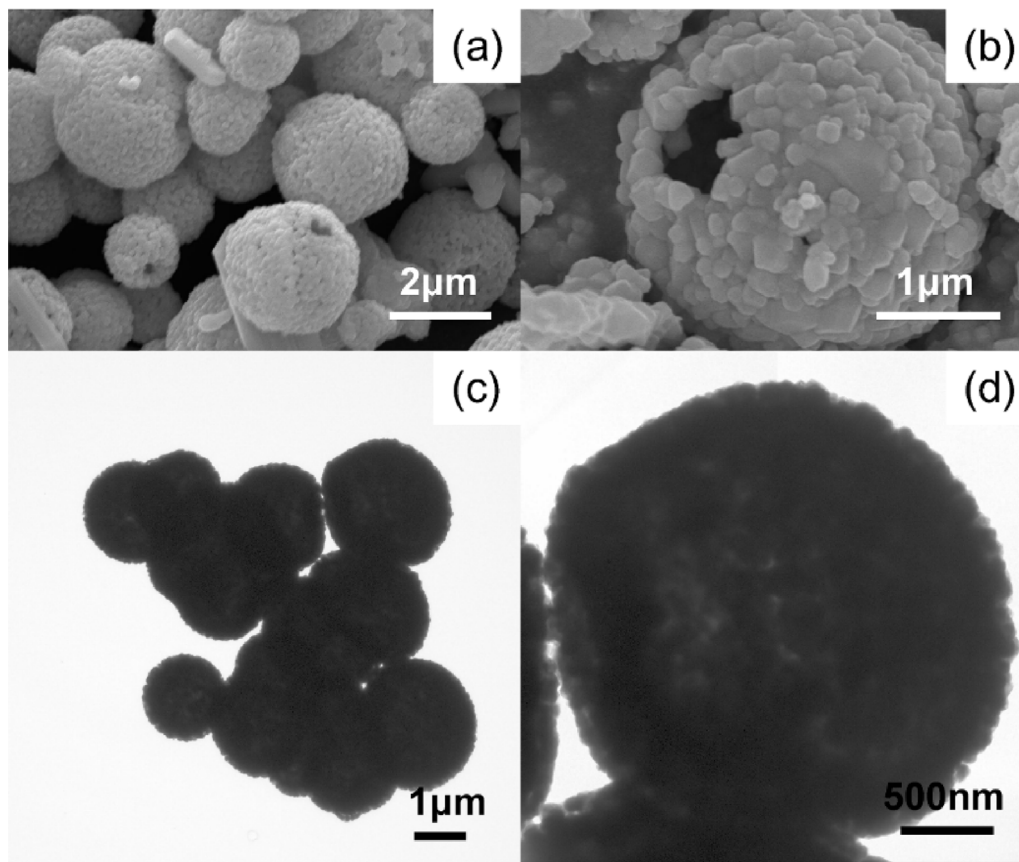


Fig. 3. FE-SEM images of (a) $\text{WO}_3/\text{g-C}_3\text{N}_4$ -4, (b) $\text{WO}_3/\text{g-C}_3\text{N}_4$ -4 with magnified scale; TEM images of (c) $\text{WO}_3/\text{g-C}_3\text{N}_4$ -4, (d) $\text{WO}_3/\text{g-C}_3\text{N}_4$ -4 with magnified scale.

intimately coated on the carbon spheres with a well dispersion. Next, WO_3 nanoparticles were formed through the hydrolysis of Na_2WO_4 , and $\text{C}_2\text{H}_4\text{N}_4$ was adsorbed on these nanoparticles. SEM and EDS elemental analysis of $\text{WO}_3\text{-C}_2\text{H}_4\text{N}_4$ -carbon spheres were showed in Fig. S4, which further demonstrated this formation mechanism. In the process of high-temperature calcination, the carbon core was decomposed into CO_2 , while the $\text{C}_2\text{H}_4\text{N}_4$ was polymerized into $\text{g-C}_3\text{N}_4$ and mingled with WO_3 . It is worth noting that any one of the precursors alone cannot construct this architecture by using the same synthetic route, Na_2WO_4 and

$\text{C}_2\text{H}_4\text{N}_4$ played a synergistic role. Here, $\text{C}_2\text{H}_4\text{N}_4$ provided an alkaline environment, and the degree of hydrolysis of Na_2WO_4 could be finely controlled similarly to a previous work [43]. By the precise addition of $\text{C}_2\text{H}_4\text{N}_4$ with 4 mmol, WO_3 was subsequently generated after the formation of carbon core. Inappropriate amounts of $\text{C}_2\text{H}_4\text{N}_4$ led to the formation of incomplete microspheres or irregular morphologies.

X-ray photoelectron spectroscopy (XPS) was used to determine the composition and oxidation state for $\text{WO}_3/\text{g-C}_3\text{N}_4$ composites. Because the content of $\text{g-C}_3\text{N}_4$ in $\text{WO}_3/\text{g-C}_3\text{N}_4$ -4 is lower than the detection

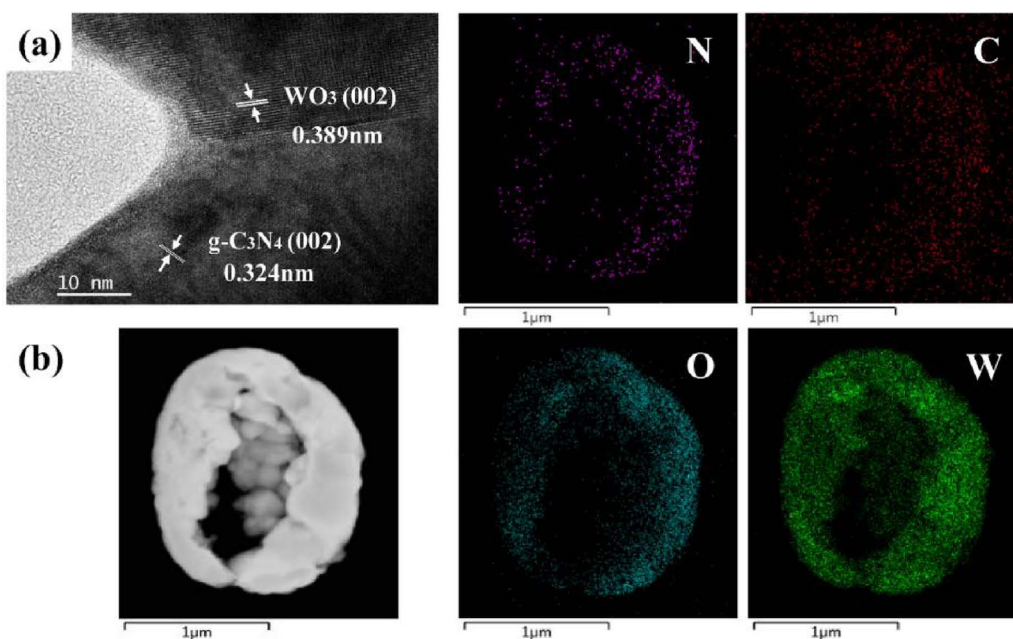


Fig. 4. (a) HAADF-STEM image and (b) EDS elemental mappings of $\text{WO}_3/\text{g-C}_3\text{N}_4$ -4.

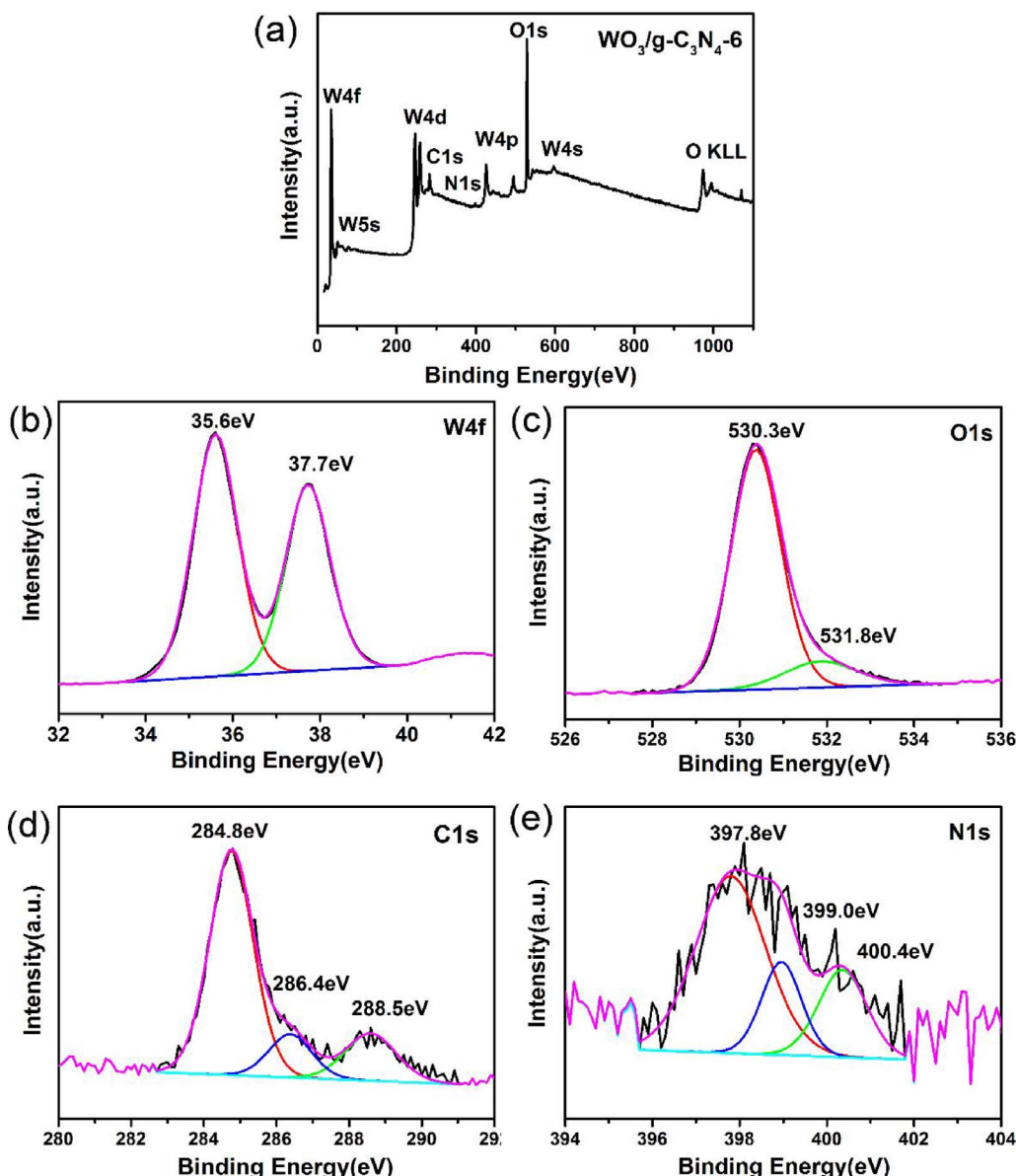


Fig. 5. (a) XPS survey spectrum of $\text{WO}_3/\text{g-C}_3\text{N}_4\text{-}6$, (b) W4f, (c) O1s, (d) C1s and (e) N1s core-level XPS spectra, respectively.

limits of XPS, $\text{WO}_3/\text{g-C}_3\text{N}_4\text{-}6$ was used for this investigation. As shown in Fig. 5a, the co-existence of C, N, O and W can be confirmed in the XPS survey spectrum. The W4f high resolution spectrum displays two typical peaks at 35.6 eV and 37.7 eV, assigned to $\text{W4f}_{4/5}$ and $\text{W4f}_{4/7}$ for W^{5+} in WO_3 [44]. For O1s in Fig. 5c, the peak can be dissociated into two peaks of 530.3 eV and 531.8 eV, corresponding to the oxygen bound species of W-O-W and W-O-H, respectively [45]. The high-resolution spectrum of C1s, demonstrated in Fig. 5d, can be divided into three peaks at 284.8 eV, 286.4 eV and 288.5 eV. The binding energy at 284.8 eV can be ascribed to the sp^2 C–C bonds, and the peak at 286.4 eV is related to sp^3 -coordinated carbon species from the defects on the $\text{g-C}_3\text{N}_4$ surface [46]. The peak at 288.5 eV could be assigned to sp^2 -bonded carbon in N-containing aromatic rings (N–C=N). Fig. 5e shows the high-resolution spectrum of N1s. Three peaks at 397.8 eV, 399.0 eV and 400.4 eV can be identified, corresponding to N- bound species of C=N=C, N–(C)₃ and C–N–H, respectively [47].

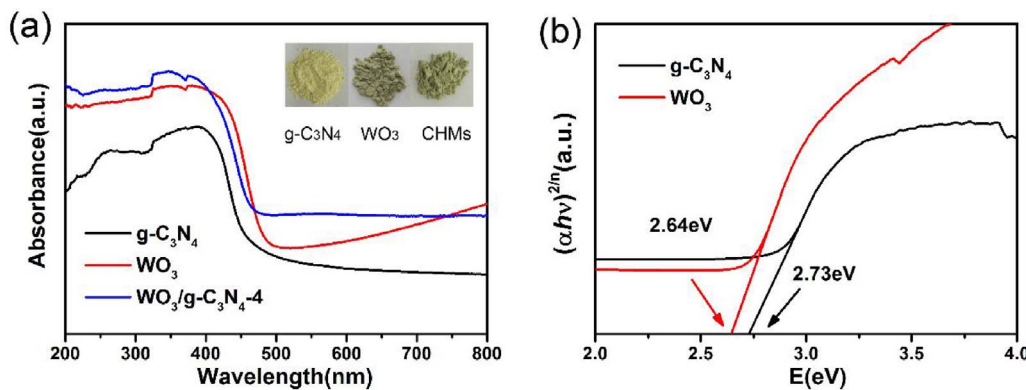
The photoabsorption behaviours of the prepared WO_3 , $\text{g-C}_3\text{N}_4$ and $\text{WO}_3/\text{g-C}_3\text{N}_4\text{-}4$ CHMs were studied by UV-vis diffuse reflectance spectra (DRS), and the results are shown in Fig. 6a. $\text{g-C}_3\text{N}_4$ exhibits high absorption from 350 nm to 470 nm due to the narrow intrinsic band gap (2.73 eV) [48]. For WO_3 , a strong absorption tail at the wavelength

longer than 500 nm can be observed, which is attributed to darker colour of WO_3 compared with $\text{g-C}_3\text{N}_4$ [49]. In addition, W^{5+} species existing on the surfaces of WO_3 have strong absorption ability in the visible light range [50]. Compared with the bare WO_3 and $\text{g-C}_3\text{N}_4$, the spectrum of $\text{WO}_3/\text{g-C}_3\text{N}_4$ CHMs is close to that of WO_3 due to the low content of $\text{g-C}_3\text{N}_4$. However, the absorption ability of $\text{WO}_3/\text{g-C}_3\text{N}_4$ CHMs increased slightly especially in the visible light region. The similar phenomenon is also existed in previous reports concerning $\text{g-C}_3\text{N}_4\text{-WO}_3$ composite [28,51]. Variety of packing modes, defects and residual groups (amino groups) resulted from the different synthetic processes would affect the absorption ability of $\text{g-C}_3\text{N}_4$. Moreover, the trace of residual carbon might be existed due to the usage of carbon spheres as the template. This also causes the elevated baseline and absorptions for $\text{WO}_3/\text{g-C}_3\text{N}_4$ CHMs.

In general, the bandgap energy of the semiconductor can be calculated with the following equation:

$$\alpha h\nu = A(h\nu - Eg)^n/2 \quad (1)$$

where α , h , Eg and A are the absorption coefficient, the photon energy, band gap and a constant, respectively. The value of n is determined by the properties of the transition in a semiconductor ($n = 1$ for direct



transition, and $n = 4$ for indirect transition) [52]. The values of n are 4 and 1 for g-C₃N₄ and WO₃, respectively. As shown in Fig. 6b, the estimated band gaps for g-C₃N₄ and WO₃ were 2.73 and 2.64, respectively. These values were in good agreement with the reported values for g-C₃N₄ and WO₃ [53,54].

3.2. Photocatalytic measurement

The photocatalytic performances of bare WO₃, g-C₃N₄ and WO₃/g-C₃N₄ composites were evaluated by degrading CFS and TC-HCl under visible light irradiation. Before the irradiation, the photocatalysts were immersed in the antibiotic solution and stirred in the dark for 30 min to reach the adsorption-desorption equilibrium. Fig. 7a shows the degradation efficiencies of CFS with different photocatalysts. In the blank experiment, the concentration of CFS remains unchanged without the photocatalyst, indicating the high stability of CFS under visible light irradiation. g-C₃N₄ and WO₃ show low photocatalytic degradation efficiencies of approximately 29% and 47%, respectively. This mainly results from the rapid recombination of electrons and holes in these two semiconductors. Compared with g-C₃N₄, WO₃ has higher degradation

efficiency due to its high VB position with strong oxidation ability and intense absorptions in the visible light region. After being combined with g-C₃N₄, the photocatalytic efficiencies of WO₃/g-C₃N₄ composites have improved significantly. As shown in Fig. 7a, WO₃/g-C₃N₄-4 CHMs exhibits the best performance in photocatalytic degradation of CFS, resulting in a degradation efficiency of 82% after 2 h of visible-light irradiation. WO₃/g-C₃N₄-2 and WO₃/g-C₃N₄-6 exhibit the similar degradation efficiencies of approximately 70% and 72%, respectively. Further increases of the content for g-C₃N₄ in the WO₃/g-C₃N₄ composites, however, would lead to the decrease of degradation efficiency. WO₃/g-C₃N₄-8 shows a photocatalytic degradation efficiency of 64%. Clearly, introduction of g-C₃N₄ enhanced the photocatalytic degradation ability of WO₃, but the content of g-C₃N₄ has significant impacts on the performance of photocatalysts and therefore has an optimal condition. This can be explained as follows: The synergistic effect of g-C₃N₄ and WO₃ has greatly promoted the separation of photoinduced electrons and holes, which has a positive effect on the photocatalytic reactions. Furthermore, WO₃/g-C₃N₄-4 CHMs with hollow architecture possesses high specific surface areas. Meanwhile, this hollow cavity provides more transmission paths for the visible light, which could

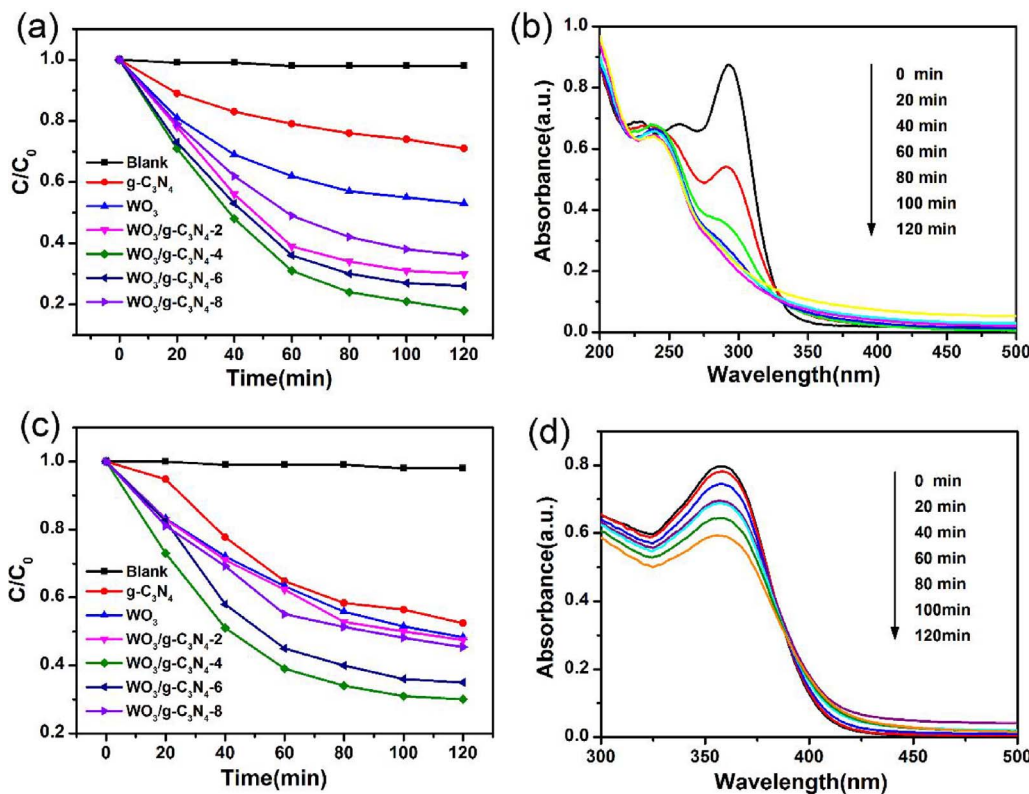


Fig. 7. (a) CFS degradation efficiency in the presence of different photocatalysts under visible light irradiation ($\lambda > 420$ nm); (b) UV-vis absorption spectra of CFS under different degradation times using WO₃/g-C₃N₄-4 CHMs; (c) TC-HCl degradation efficiency in the presence of different photocatalysts under visible light irradiation ($\lambda > 420$ nm); (d) UV-vis absorption spectra of TC-HCl under different degradation times using WO₃/g-C₃N₄-4 CHMs.

improve the absorption and use of radiation energy. With too much or too little g-C₃N₄, the composites were imperfect and irregular aggregates were generated. The specific surface areas and number of active sites were reduced, eventually leading to the reduction of photocatalytic efficiencies.

Fig. 7b shows the UV-vis absorption spectra of CFS under different irradiation times in the presence WO₃/g-C₃N₄-4 CHMs. With the increase of time, the absorption of CFS gradually decreased, which indicates that CFS was gradually degraded under visible light. A pseudo-first-order reaction kinetics equation was also used to explain the experiments quantitatively. As shown in Fig. S6 and Table S1, photocatalysis is well described by the model, WO₃/g-C₃N₄-4 CHMs showed the highest photocatalytic activity with $k_{app} = 0.0164 \text{ min}^{-1}$.

In addition to CFS, the degradation of TC-HCl under visible light was also conducted. As shown in Fig. 7c, TC-HCl also exhibited high stability under visible light irradiation. Unlike the case of CFS, g-C₃N₄ and WO₃ showed a better photocatalytic degradation efficiency towards TC-HCl, which attained 47% and 52%, respectively. Interestingly, the improvement of degradation efficiencies differed, increasing 18% and 5% for g-C₃N₄ and WO₃, respectively. In other words, the upgrade rate decreased. WO₃/g-C₃N₄-4 CHMs also displayed the best performance in photocatalytic degradation of TC-HCl, providing a degradation efficiency of 70% after 2 h visible-light irradiation. Meanwhile, the degradation efficiencies of the WO₃/g-C₃N₄-2 and WO₃/g-C₃N₄-8 did not show clear improvement compared with WO₃. This was mainly the result of the imperfect morphologies and the lack of active sites. Fig. 7d presents the UV-vis absorption spectra of TC-HCl under different irradiation times by using WO₃/g-C₃N₄-4 CHMs. The absorption of TC-HCl was gradually decreased with the increase of time, indicating the gradual degradation of TC-HCl under visible light. Like the similar trends for CFS degradation, the pseudo-first-order reaction kinetics equation of TC-HCl degradation declared the highest apparent rate constant of $k_{app} = 0.0120 \text{ min}^{-1}$ for WO₃/g-C₃N₄-4 CHMs.

It should be noted that the degradation abilities of g-C₃N₄ and WO₃ on TC-HCl are higher than that of CFS, whereas the WO₃/g-C₃N₄-4 CHMs is just the opposite; the degradation efficiency of TC-HCl is lower than that of CFS. This may result from the different degradation products of the two antibiotics: the degradation products with high stability for TC-HCl occupied the active sites on the photocatalyst, whereas the photodegradation reaction had thus been inhibited [55,56]. The more degradation products, the more serious the inhibition. Therefore, the upgrade rate for the degradation of TC-HCl on WO₃ was decreased to 5% due to its high degradation efficiency compared with g-C₃N₄. Eventually, although the degradation efficiencies of WO₃/g-C₃N₄-4 CHMs for both of the CFs and TC-HCl are higher than that of WO₃, which increase by 35% and 18%, many active sites were occupied in the process for degradation of TC-HCl, and WO₃/g-C₃N₄-4 CHMs exhibited lower degradation efficiency for TC-HCl compared with that of CFS. Meanwhile, the pseudo-first-order reaction kinetics equation exhibited similar results: the apparent rate constants for TC-HCl degradation on g-C₃N₄ and WO₃ are higher than that of CFS. For the WO₃/g-C₃N₄ composites, however, the values are all reduced.

Fig. 8 shows the TOC removal of CFS and TC-HCl as a function of reaction time. Obviously, the TOC removal of CFS and TC-HCl by photocatalyst was significantly lower than that of degradation, and the trend of TOC removal after 2 h is still maintained. This is mainly due to the intermediate products generated during degradation, which didn't convert into CO₂ thoroughly. Some of the products remained in the system and could be degraded in more time. After 2 h irradiation, the TOC removal of CFS and TC-HCl by WO₃/g-C₃N₄-4 CHMs reached 47.9% and 37.6%, which were significantly higher than that of the g-C₃N₄ and WO₃. This illustrated that the photocatalytic activity and mineralization ability of WO₃/g-C₃N₄-4 CHMs are obviously enhanced compared with the components.

The reusability and stability of the photocatalyst were investigated. As shown in Fig. 9a, there is no significant decrease in the

photocatalytic efficiency after four cycles, confirming the high stability of WO₃/g-C₃N₄-4 CHMs during the photocatalytic reaction. Fig. 9b shows the comparisons of XRD patterns of WO₃/g-C₃N₄-4 CHMs before and after photocatalytic reaction. It is clear that no change occurred, demonstrating the superior chemical stability of the photocatalyst.

3.3. Mechanism considerations

The adsorption ability of a photocatalyst has an important influence on its photocatalytic activity. Therefore, the adsorption performance of WO₃/g-C₃N₄-4 CHMs was evaluated. Three kinetic models, including the Lagergren-first-order, pseudo-second-order, and Weber and Morris were applied to study the adsorption process of CFS and TC-HCl. The mathematical equations of these kinetic models are represented as follows:

$$\log(q_e - q_t) = \log q_e - \frac{k_1}{2.303}t \quad (2)$$

$$\frac{t}{q_t} = \frac{1}{k_2 q_e^2} + \frac{1}{q_e} t \quad (3)$$

$$q_t = k_{id} t^{1/2} + c \quad (4)$$

In the above equations, q_e and q_t are the amount of antibiotics adsorbed (mg/g) at equilibrium and at a given time of adsorption (min), respectively. k_1 (min^{-1}) is the rate constant of Lagergren-first-order kinetic model [57], k_2 ($\text{g mg}^{-1} \text{min}^{-1}$) is the rate constant of pseudo-second-order kinetic model for adsorption [58], k_{id} ($\text{mg g}^{-1} \text{min}^{-1/2}$) is the intraparticle diffusion rate constant, and c (mg g^{-1}) is the intercept [59].

The results of adsorption experiments with the linearized plots of three models are displayed in Fig. 10, and the corresponding rate constants are listed in Table S2. For CFS, the WO₃/g-C₃N₄-4 CHMs reached an adsorption of 6.90 mg/g after 60 min, corresponding to 99% of adsorption saturation. In addition, the adsorption of TC-HCl was 9.64 mg/g after 60 min, which also reached 99% of adsorption saturation. The plots of actual adsorption data for both antibiotics coincided well with the pseudo-second-order kinetic model with the high correlation coefficients ($R^2 > 0.995$). This result indicates that the chemical adsorption is the rate-limiting factor for the adsorption process [60]. In general, a high absorption performance for photocatalyst implies a high degradation efficiency. TC-HCl molecules are more likely to form chemical bonds or hydrogen bonds with the absorbent, whereas CFS has high stability. Therefore, photocatalytic degradation efficiencies towards TC-HCl on g-C₃N₄ and WO₃ are higher than that of the CFS when the occupancy rates for active sites are low, which is in accordance with the above experimental results. When the active sites on photocatalysts were occupied to some degree, the photocatalytic reactions were seriously inhibited.

To further explore the photocatalytic mechanism of the composite system, the test of transient photocurrent response and EIS Nyquist plots were conducted to investigate the separation and migration of the light-induced electrons and holes in the photocatalysts. Fig. 11a shows the transient photocurrent intensities for WO₃, g-C₃N₄ and WO₃/g-C₃N₄ composites with repeating on-off cycles under intermittent irradiation. It is clear that the composites showed enhanced photocurrent intensities and the course could repeat steadily. There is an optimum for the composites, however; WO₃/g-C₃N₄-4 CHMs has the highest photocurrent intensity, which indicates the most efficient separation of electron-hole pairs. The current increased dramatically when the catalysts were irradiated, and photocurrents rapidly decreased to zero as soon as the light was turned off. Fig. 11b describes the EIS Nyquist plots of WO₃, g-C₃N₄ and WO₃/g-C₃N₄ composites. A smaller radius of the arc in the spectra manifests a smaller charge transfer resistance for the photoelectrodes as a result of the more effective separation of the photogenerated electron-hole pairs and faster interfacial charge

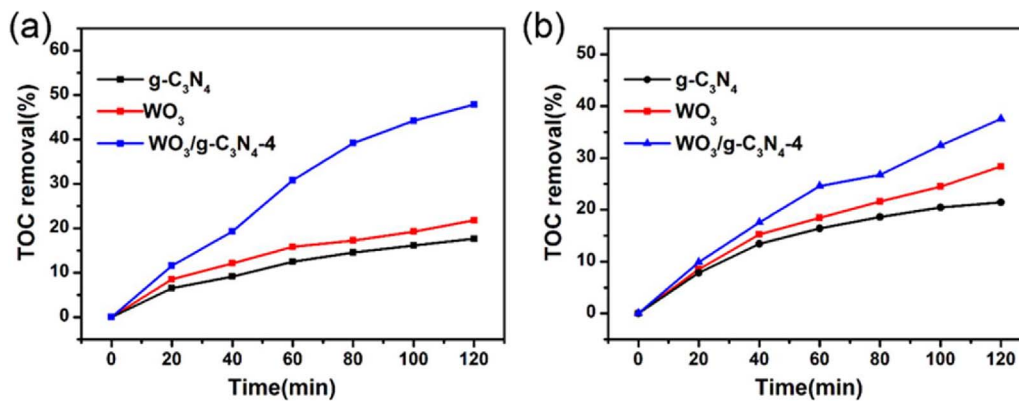


Fig. 8. TOC removal of (a) CFS, (b) TC-HCl in the presence of different photocatalysts under visible light irradiation ($\lambda > 420 \text{ nm}$).

transport. As shown, $\text{WO}_3/\text{g-C}_3\text{N}_4$ -4 CHMs exhibits a similar trend to that of the photocurrent experiment, and the arc radius is the smallest among the $\text{WO}_3/\text{g-C}_3\text{N}_4$ composites and their sole components. The equivalent circuit (inset in Fig. 11b) of the device was also employed for further analyzing of the impedance spectra, which was fitted using the ZSimpWin software. R_s is the electrolyte solution resistance, CPE is the constant phase element for the electrode and electrolyte interface, and R_{ct} is the interfacial charge transfer resistance across the electrode/electrolyte [61]. It signified that $\text{WO}_3/\text{g-C}_3\text{N}_4$ -4 CHMs exhibited the fastest interfacial charge transfer and the most efficient separation of photo-generated charge carriers. Based on these analyses, the high photocatalytic activity of $\text{WO}_3/\text{g-C}_3\text{N}_4$ -4 CHMs can be declared.

Photogenerated charge carriers are the active species for photocatalytic reactions; thus, investigating the survival time of the electron-hole pairs is fundamental. The lifetimes of the carriers for WO_3 , $\text{g-C}_3\text{N}_4$ and $\text{WO}_3/\text{g-C}_3\text{N}_4$ CHMs were determined by the photoluminescence (PL) decay profiles. As shown in Fig. 12a and Table S3, the transient PL decay trace of the bare WO_3 shows a PL lifetime of $\sim 1.62 \text{ ns}$, while the PL lifetime for $\text{WO}_3/\text{g-C}_3\text{N}_4$ CHMs attains $\sim 2.23 \text{ ns}$. Numerous interfaces in the intact hollow microspheres accelerate the transfer of photogenerated electrons from the CB of WO_3 to VB of $\text{g-C}_3\text{N}_4$, which contributed to a long PL lifetime [62]. The prolonged lifetime of charge carriers signifies improved reaction abilities, and the photocatalytic degradation efficiency of $\text{WO}_3/\text{g-C}_3\text{N}_4$ CHMs is enhanced, which is in accordance with results in the photocatalytic experiments. $\text{g-C}_3\text{N}_4$ exhibited the longest PL lifetime of $\sim 4.46 \text{ ns}$, however, but its photodegradation efficiency is low. Therefore, photoluminescence (PL) spectrum is used for demonstration of the recombination of charge carriers. As shown in Fig. 12b, $\text{g-C}_3\text{N}_4$ displays the strongest PL intensity, indicating the highest recombination rate of photogenerated electron-hole pairs among these catalysts. This is the reason that $\text{g-C}_3\text{N}_4$ displayed the lowest photodegradation abilities with the longest PL lifetime. Compared with WO_3 , $\text{WO}_3/\text{g-C}_3\text{N}_4$ CHMs exhibits weaker PL emission intensities due to the great inhibition for the recombination of

photogenerated electron-hole pairs (insert in Fig. 12b). The photocatalytic efficiencies is thus improved. The highest photocatalytic efficiency of $\text{WO}_3/\text{g-C}_3\text{N}_4$ CHMs was the synthetic actions of the lifetime of the electron-hole pairs and their recombination.

It is well known that $\cdot\text{OH}$, $\cdot\text{O}_2^-$ and h^+ are three typical active species for the degradation of pollutants. To investigate the photocatalytic mechanism of $\text{WO}_3/\text{g-C}_3\text{N}_4$ composites and the role of various active species in the photocatalytic process, a scavenger was introduced in the degradation of CFS under visible light in the presence of $\text{WO}_3/\text{g-C}_3\text{N}_4$ -4. In these experiments, isopropanol (IPA) was used to eliminate the hydroxyl radical ($\cdot\text{OH}$). Superoxide radical ($\cdot\text{O}_2^-$) and hole (h^+) were removed by benzoquinone (BQ) and ethylenediaminetetraacetic acid (EDTA), respectively. Fig. 13 shows the effects of three scavengers on the photocatalytic efficiencies. When IPA was added, the catalytic efficiency was reduced to 45%, suggesting that hydroxyl radicals ($\cdot\text{OH}$) contribute to the degradation of CFs. The photocatalytic efficiency did not change significantly when BQ was added, however, revealing that $\cdot\text{O}_2^-$ does not play an important role in the degradation. When EDTA was added, the photocatalytic efficiency was also significantly reduced by 28%. It indicates that h^+ is one of the major active species. In conclusion, $\cdot\text{OH}$ and h^+ are the major reactive species for the degradation of CFS on $\text{WO}_3/\text{g-C}_3\text{N}_4$ composites.

According to the results of the active species trapping experiments, the possible photocatalytic mechanism of $\text{WO}_3/\text{g-C}_3\text{N}_4$ CHMs can be described in Scheme 2. The band edge position of CB and VB of semiconductors can be calculated according to the following empirical formulas [63]:

$$E_{VB} = X - E_e + 0.5Eg \quad (5)$$

$$E_{CB} = E_{VB} - Eg \quad (6)$$

where X is the absolute electronegativity of the semiconductor. For WO_3 and $\text{g-C}_3\text{N}_4$, the X values are 6.59 eV and 4.67 eV, respectively. E_e is a constant of approximately 4.5 eV, representing the energy of free

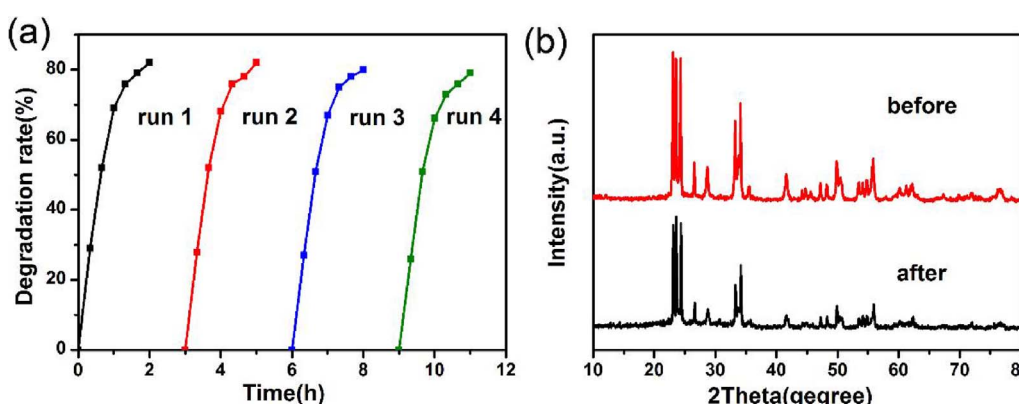


Fig. 9. (a) Photodegradation of CFS in solution for 4 cycles using $\text{WO}_3/\text{g-C}_3\text{N}_4$ -4 CHMs under visible light irradiation ($\lambda > 420 \text{ nm}$); (b) The comparisons of XRD patterns of $\text{WO}_3/\text{g-C}_3\text{N}_4$ -4 CHMs before and after photocatalytic degradation.

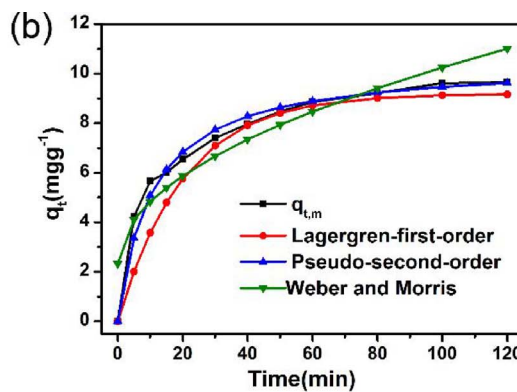
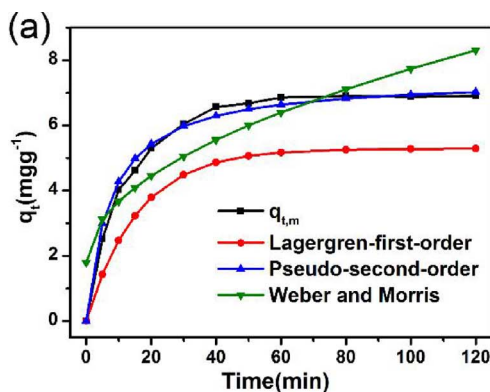


Fig. 10. Sorption kinetics of (a) CFS, (b) TC-HCl adsorption by $\text{WO}_3/\text{g-C}_3\text{N}_4\text{-}4$ CHMs in dark.

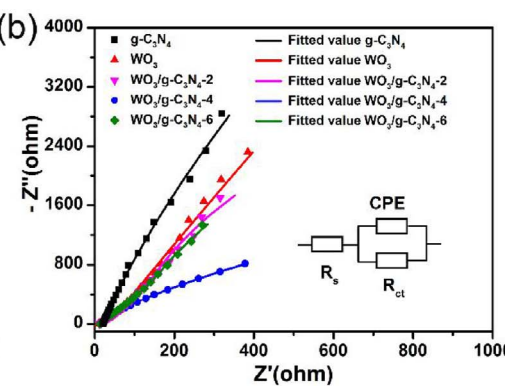
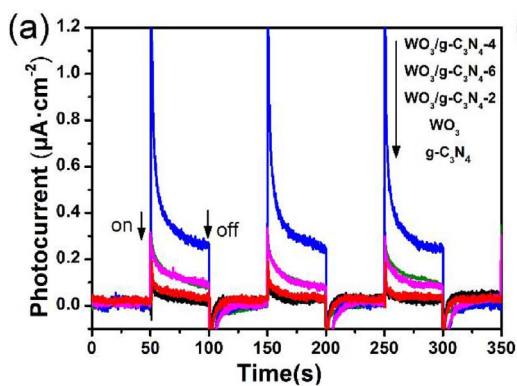


Fig. 11. (a) Transient photocurrent responses and (b) Electrochemical impedance spectra (EIS) of WO_3 , $\text{g-C}_3\text{N}_4$ and $\text{WO}_3/\text{g-C}_3\text{N}_4$ composites.

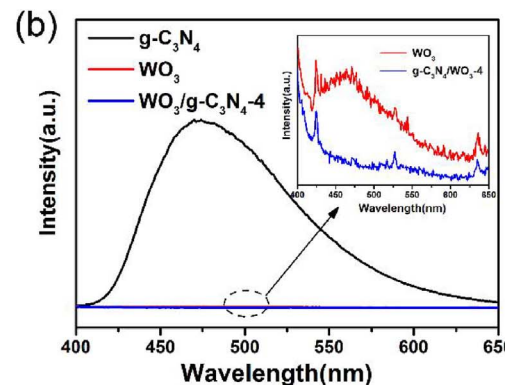
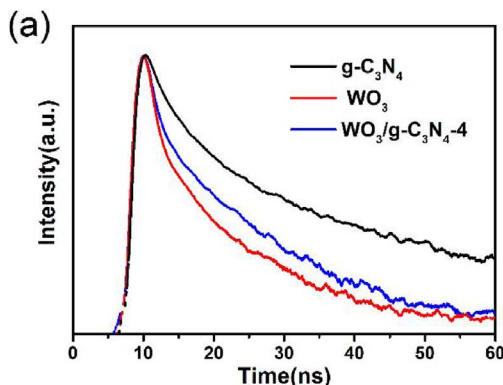


Fig. 12. (a) Photoluminescence decay traces of WO_3 and $\text{WO}_3/\text{g-C}_3\text{N}_4$ composite, (b) Photoluminescence (PL) spectra of WO_3 , $\text{g-C}_3\text{N}_4$ and $\text{WO}_3/\text{g-C}_3\text{N}_4\text{-}4$ CHMs.

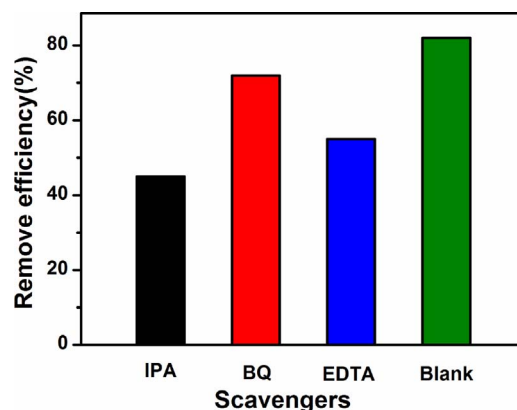
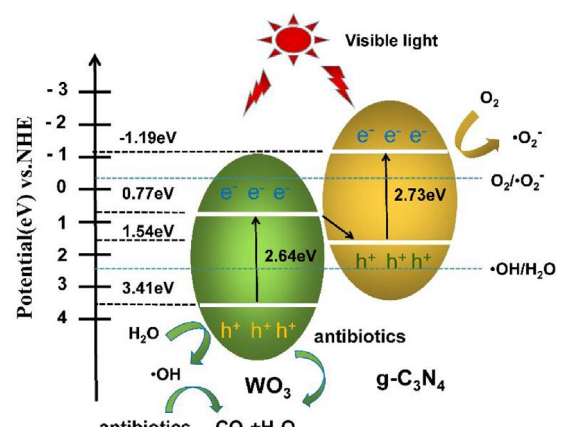


Fig. 13. Effects of different scavengers on the photocatalytic efficiency of $\text{WO}_3/\text{g-C}_3\text{N}_4\text{-}4$ CHMs.



Scheme 2. Schematic diagram of the possible photocatalytic mechanism of the $\text{WO}_3/\text{g-C}_3\text{N}_4$ CHMs.

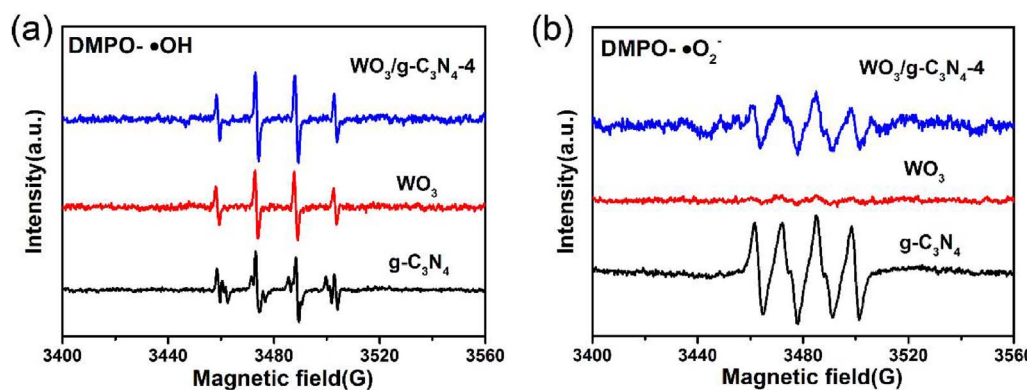


Fig. 14. ESR spectra of (a) DMPO-·OH adduct and (b) DMPO-·O₂⁻ adduct over WO₃, g-C₃N₄ and WO₃/g-C₃N₄-4 CHMs after visible-light irradiation.

electrons on the hydrogen scale. E_g is the band gap energy of the semiconductor, which was obtained in Fig. 6b. The E_g of WO₃ and g-C₃N₄ are 2.64 eV and 2.73 eV, respectively. Therefore, the E_{VB} of WO₃ and g-C₃N₄ are calculated to be 3.41 eV and 1.54 eV, respectively. Accordingly, the E_{CB} of WO₃ and g-C₃N₄ are 0.77 eV and -1.19 eV. For WO₃, the VB position of WO₃ is more positive than the standard redox potential of ·OH/H₂O (2.4 eV vs. NHE), and thus the photoinduced holes in VB can oxidize the adsorbed H₂O molecules to ·OH. However, the position of CB of WO₃ is more positive than the potential of O₂/·O₂⁻ (-0.33 eV vs. NHE), the photogenerated electrons on the CB of WO₃ cannot reduce O₂ to ·O₂⁻ radicals. For g-C₃N₄, the photogenerated electrons on the CB can react with O₂ and generate ·O₂⁻ radicals, while the photoexcited holes in the VB cannot generate ·OH due to the lower VB position compared with the standard redox potential of ·OH/H₂O (2.4 eV vs. NHE). Based on the above analysis, a Z-Scheme heterojunction photocatalytic system can be proposed [64–66]. Under the visible light irradiation, electrons on the VB of WO₃ and g-C₃N₄ can be excited and transfer to the CB, resulting in the photogenerated electron-hole pairs. However, electrons cannot accumulate on the CB of WO₃ since the position of CB of WO₃ is more positive, therefore the electrons on the CB of WO₃ transfer to the VB of g-C₃N₄ and eventually combine with the photogenerated holes on the VB of g-C₃N₄. As a result, the remaining holes for WO₃ accumulate on the VB for generation of ·OH, and the photogenerated electrons accumulate on the CB of g-C₃N₄ for generation of ·O₂⁻.

In order to further verification of the direct Z-scheme mechanism, ESR measurements using 5,5-dimethyl-1-pyrroline-N-oxide (DMPO) as the trapping agent were conducted for investigation of ·OH and ·O₂⁻ radicals in WO₃, g-C₃N₄ and WO₃/g-C₃N₄ CHMs photocatalytic systems. As shown in Fig. 14a, four characteristic peaks with intensity ratio of 1:2:2:1 for DMPO-·OH adducts were observed in all of the systems. This indicates that ·OH radicals are generated on the three samples after irradiation. However, the energy band theory declares that ·OH could not be produced by g-C₃N₄. According to the previous report [67], ·OH may be generated by further reduction of ·O₂⁻, which is an indirect way. It is worth noting that the intensity of DMPO-·OH signals for WO₃/g-C₃N₄ CHMs is obviously stronger than that of the pure g-C₃N₄ and WO₃, implying that the amount of ·OH radicals produced on WO₃/g-C₃N₄ heterostructured surfaces is more than that of the g-C₃N₄ and WO₃. This demonstrates the accumulation of holes on the VB of WO₃ in WO₃/g-C₃N₄ CHMs. The six characteristic peaks of DMPO-·O₂⁻ adducts were presented for g-C₃N₄ and WO₃/g-C₃N₄ CHMs in Fig. 14b. No obvious signals are observed for pure WO₃, which is accorded with the position of its CB. Therefore, the type-II heterojunction could be ruled out for WO₃/g-C₃N₄ CHMs. Moreover, WO₃ is the main component with the low content of g-C₃N₄ for WO₃/g-C₃N₄ CHMs. This results in the limited generation of ·O₂⁻, and the intensity of DMPO-·O₂⁻ signal for WO₃/g-C₃N₄ CHMs is thus weaker than that of the bare and bulk of g-C₃N₄. This Z-Scheme photocatalyst retains the intense oxidation and reduction abilities for WO₃ and g-C₃N₄ without any variation in the

oxidation and reduction potential. Combined with the excellent separation and transfer of photogenerated electron-hole pairs, the degradation towards antibiotics is greatly enhanced.

4. Conclusions

In summary, WO₃/g-C₃N₄ CHMs with intact and well-defined structures were prepared by a precisely controlled in situ hydrolysis and polymerization process. Under visible-light irradiation, the WO₃/g-C₃N₄ CHMs exhibited enhanced photocatalytic degradation performance compared with the bare WO₃, g-C₃N₄ and their imperfect composites, which gives a degradation efficiency of 82% for TC-HCl and 70% for CFS within 2 h. The significantly enhanced photocatalytic activity benefited from the particular structure of WO₃/g-C₃N₄ CHMs. The hollow structure allows the trapping of the incident light for a longer time under irradiation, which facilitates the effective utilization of photons. In addition to the hollow structure and high specific areas, the shells of the microspheres were constructed by the well-distributed WO₃ and g-C₃N₄ nanoparticles. Numerous interfaces were thus generated, and elegant heterojunctions could be built with highly exposed oxidation-reduction active sites. By virtue of this special architecture, the effective separation of photoinduced electron-hole pairs and long survival time of charge carriers were simultaneously realized. In combination with the traits of the Z-Scheme system, it retains the original oxidation and reduction abilities of the components without changing the oxidation and reduction potentials. All the requirements for an excellent photocatalyst are present. It is anticipated that this particular design could also be used to construct other heterojunctions. Moreover, it may provide new inspirations for improving the activities of photocatalysts.

Acknowledgments

We are grateful to the National Nature Science Foundation of China (51303083, 21473091, 21603183), the Nature Science Foundation of Jiangsu Province (BK20130759), the Fundamental Research Funds for the Central Universities (30917011310), the Jiangsu Postdoctoral Science Foundation (1601062B) and A Project Funded by the Priority Academic Program Development of Jiangsu Higher Education Institutions (PAPD) for financial support.

Appendix A. Supplementary data

Supplementary data associated with this article can be found, in the online version, at <http://dx.doi.org/10.1016/j.apcatb.2017.08.070>.

References

- [1] R. Daghrir, P. Drogui, Environ. Chem. Lett. 11 (2013) 209–227.
- [2] R. Capita, C. Alonso-Calleja, Crit. Rev. Food Sci. 53 (2013) 11–48.
- [3] Y. Gao, Y. Li, L. Zhang, H. Huang, J.J. Hu, S.M. Shah, X.G. Su, J. Colloid Interface

- Sci. 368 (2012) 540–546.
- [4] H. Kim, Y.S. Hwang, V.K. Sharma, J. Chem. Eng. 255 (2014) 23–27.
- [5] J. Li, N. Zhang, D.H.L. Ng, J. Mater. Chem. A 3 (2015) 21106–21115.
- [6] G. Ghosh, S. Hanamoto, N. Yamashita, X. Huang, H. Tanaka, Pollution 2 (2016) 131–139.
- [7] K. Micoine, P. Persich, J. Llaveria, H. Lam, Chem. Eur. J. 19 (2013) 7370–7383.
- [8] M. Yan, Y. Hua, F. Zhu, W. Gu, J.H. Jiang, H.Q. Shen, W.D. Shi, Appl. Catal. B: Environ. 202 (2017) 518–527.
- [9] C. Li, G. Chen, J. Sun, J.C. Rao, Z.H. Han, Y.D. Hu, W.N. Xing, C.M. Zhang, Appl. Catal. B: Environ. 188 (2016) 39–47.
- [10] L.Q. Mai, Q.J. Zhang, C.W. Nan, Adv. Mater. 29 (2017) 1601694.
- [11] J. Han, X.Z. Zheng, L.W. Zhang, H.B. Fu, J.M. Chen, Environ. Sci.: Nano 4 (2017) 834–842.
- [12] L.W. Zhang, H.B. Fu, Y.F. Zhu, Adv. Funct. Mater. 18 (2008) 2180–2189.
- [13] W.K. Wang, J.J. Chen, W.W. Li, D.N. Pei, X. Zhang, H.Q. Yu, ACS Appl. Mater. Interfaces 7 (2015) 20349–20359.
- [14] Q. Chen, Y. Xin, X. Zhu, Electrochim. Acta 186 (2015) 34–42.
- [15] M. Ahmad, S.Y. Ying, A. Nisar, H.Y. Sun, W.C. Shen, M. Wei, J. Zhu, J. Mater. Chem. 21 (2011) 7723–7729.
- [16] X.J. Liu, L.K. Pan, Q.F. Zhao, T. Lv, G. Zhu, T.Q. Chen, T. Lu, Z. Sun, C.Q. Sun, J. Chem. Eng. 183 (2012) 238–243.
- [17] H. Moussa, E. Girot, K. Mozet, H. Alem, G. Medjahdi, R. Schneider, Appl. Catal. B: Environ. 185 (2016) 11–21.
- [18] M.M. Khan, S.A. Ansari, M.E. Khan, M.O. Ansari, B.K. Min, M.H. Cho, New J. Chem. 39 (2015) 2758–2766.
- [19] F. Amano, E. Ishinaga, A. Yamakata, J. Phys. Chem. C 117 (2013) 22584–22590.
- [20] W. Li, P. Da, Y. Zhang, Y.C. Wang, X. Lin, X.G. Gong, G.F. Zheng, ACS Nano 8 (2014) 11770–11777.
- [21] A.J.E. Rettie, K.C. Klavetter, J.F. Lin, A. Dolocan, H. Celio, A. Ishiekwene, H.L. Bolton, K.N. Pearson, N.T. Hahn, C. Buddie Mullins, Chem. Mater. 26 (2014) 1670–1677.
- [22] K.H. He, J. Xie, X.Y. Luo, J.Q. Wen, S. Ma, X. Li, Y.P. Fang, X.C. Zhang, Chin. J. Catal. 38 (2017) 240–252.
- [23] M. Zhang, X.J. Bai, D. Liu, J. Wang, Y.F. Zhu, Appl. Catal. B: Environ. 164 (2015) 77–81.
- [24] M. Zhang, W.J. Jiang, D. Liu, J. Wang, Y.F. Liu, Y.Y. Zhu, Y.F. Zhu, Appl. Catal. B: Environ. 183 (2016) 263–268.
- [25] J.Q. Wen, J. Xie, X.B. Chen, X. Li, Appl. Surf. Sci. 391 (2017) 72–123.
- [26] L.F. Cui, X. Ding, Y.G. Wang, H.C. Shi, L.H. Huang, Y.H. Zuo, S.F. Kang, Appl. Surf. Sci. 391 (2017) 202–210.
- [27] Z. Jin, N. Murakami, T. Tsubota, T. Ohnoa, Appl. Catal. B: Environ. 150 (2014) 479–485.
- [28] K. Katsumata, R. Motoyoshi, N. Matsushita, K. Okada, J. Hazard. Mater. 260 (2013) 475–482.
- [29] S.B. Yang, Y.J. Gong, J.S. Zhang, L. Zhan, L.L. Ma, Z.Y. Fang, R. Vajtai, X.C. Wang, Adv. Mater. 25 (2013) 2452–2456.
- [30] P. Niu, L. Zhang, G. Liu, H.M. Cheng, Adv. Funct. Mater. 22 (2012) 4763–4770.
- [31] T. Simon, N. Bouchonville, M.J. Berr, A. Vaneski, A. Adrović, D. Volbers, R. Wyrwich, M. Doblinger, A.S. Susha, A.L. Rogach, F. Jackel, J.K. Stolarczyk, J. Feldmann, Nat. Mater. 13 (2014) 1013–1018.
- [32] D.B. Xu, W.D. Shi, C.J. Song, M. Chen, S.B. Yang, W.Q. Fan, B.Y. Chen, Appl. Catal. B: Environ. 191 (2016) 228–234.
- [33] X. Li, J.G. Yu, M. Jaroniec, Chem. Soc. Rev. 45 (2016) 2603–2636.
- [34] M.H. Pham, C.T. Dinh, G.T. Vuong, N.D. Ta, T.O. Do, Phy. Chem. Chem. Phys. 16 (2014) 5937–5941.
- [35] J.J. Yuan, X.K. Zhang, H.D. Li, K. Wang, S.Y. Gao, Z. Yin, H.J. Yu, X.R. Zhu, Z.Z. Xiong, Y.M. Xie, Catal. Commun. 60 (2015) 129–133.
- [36] W.G. Tu, Y. Zhou, S.C. Feng, Q.F. Xu, P. Li, X.Y. Wang, M. Xiao, Z.G. Zou, Chem. Commun. 51 (2015) 13354–13357.
- [37] W.G. Tu, Y. Zhou, H. Li, P. Li, Z.G. Zou, Nanoscale 7 (2015) 14232–14236.
- [38] Y. Zhang, Y. Zhou, L.Q. Tang, M. Wang, W.G. Li, J.M. Liu, Z.G. Zou, Part. Part. Syst. Char. 33 (2016) 583–588.
- [39] X.C. Wang, K. Maeda, A. Thomas, K. Takanabe, G. Xin, J.M. Carlsson, K. Domén, M. Antonietti, Nat. Mater. 8 (2009) 76–80.
- [40] Y.J. Cui, Z.X. Ding, X.Z. Fu, X.C. Wang, Angew. Chem. Int. Ed. 51 (2012) 11814–11818.
- [41] J.H. Sun, J.S. Zhang, M.W. Zhang, M. Antonietti, X.Z. Fu, X.C. Wang, Nat. Commun. 16 (2012) 1–7.
- [42] S.C. Yan, Z.S. Li, Z.G. Zou, Langmuir 25 (2009) 10397–10401.
- [43] C.Y. Lee, S.J. Kim, I.S. Hwang, J.H. Lee, Sens. Actuators B-Chem. 142 (2009) 236–242.
- [44] Y.G. Li, X.L. Wei, X.Y. Yan, J.T. Cai, A.N. Zhou, M.R. Yan, K.Q. Liu, Phys. Chem. Chem. Phys. 18 (2016) 10255–10261.
- [45] Z. Liu, Z.G. Zhao, M. Miyachi, J. Phys. Chem. C 113 (2009) 17132–17137.
- [46] L. Ge, C. Han, J. Liu, Y.F. Li, Appl. Catal. A: Gen. 409 (2011) 215–222.
- [47] F. Dong, Z.W. Zhao, T. Xiong, Z.L. Ni, W.D. Zhang, Y.J. Sun, W.K. Ho, ACS Appl. Mater. Interfaces 5 (2013) 11392–11401.
- [48] J.Q. Tian, R. Ning, Q. Liu, A.M. Asiri, A.O. Al Youbi, X.P. Sun, ACS Appl. Mater. Interfaces 6 (2014) 1011–1017.
- [49] W. Morales, M. Cason, O. Aina, N.R.D. Tacconi, K. Rajeshwar, J. Am. Chem. Soc. 130 (2008) 6318–6319.
- [50] M.S. Bazarjani, M. Hojaberdi, K. Morita, G.Q. Zhu, G. Cherkashinin, C. Fasel, T. Herrmann, H. Breitzke, A. Gurlo, R. Riedel, J. Am. Chem. Soc. 135 (2013) 4467–4475.
- [51] S.F. Chen, Y.F. Hu, S.G. Meng, X.L. Fu, Appl. Catal. B: Environ. 150–151 (2014) 564–573.
- [52] J.H. Liu, Y.W. Zhang, L.H. Lu, G. Wu, W. Chen, Chem. Commun. 48 (2012) 8826–8828.
- [53] Y. Su, Z.K. Han, L. Zhang, W.Z. Wang, M.Y. Duan, X.M. Li, Y.L. Zheng, Y.G. Wang, X.L. Lei, Appl. Catal. B: Environ. 217 (2017) 108–114.
- [54] L. Ge, C.C. Han, J. Liu, Appl. Catal. B: Environ. 108–109 (2011) 100–107.
- [55] M.J. Zhou, D.L. Han, X.L. Liu, C.C. Ma, H.Q. Wang, Y.F. Tang, P.W. Huo, W.D. Shi, Y.S. Yan, J.H. Yang, Appl. Catal. B: Environ. 172 (2015) 174–184.
- [56] Y. Ma, N. Gao, C. Li, Environ. Eng. Sci. 29 (2012) 357–362.
- [57] E. Demirbas, N. Dizge, M.T. Sulak, M. Kobya, J. Chem. Eng. 148 (2009) 480–487.
- [58] W.S. WanNgah, S. Fatinathan, J. Chem. Eng. 143 (2008) 62–72.
- [59] X.M. Peng, D.P. Huang, T.O. Wuba, D.F. Fu, J.L. Huang, J. Colloid. Interfaces Sci. 430 (2014) 272–282.
- [60] H.Y. Zhu, R. Jiang, L. Xiao, G.M. Zeng, Bioresour. Technol. 101 (2010) 5063–5069.
- [61] J. Xu, L.W. Zhang, R. Shi, Y.F. Zhu, J. Mater. Chem. A 1 (2013) 14766–14772.
- [62] H.J. Li, Y.Y. Gao, Y. Zhou, Y. Zhou, F.T. Fan, Q.T. Ha, Q.F. Xu, X.Y. Wang, M. Xiao, C. Li, Z.G. Zou, Nano Lett. 16 (2016) 5547–5552.
- [63] Z.H. Chen, W.L. Wang, Z.G. Zhang, X.M. Fang, J. Phys. Chem. C 117 (2013) 19346–19352.
- [64] B.C. Zhu, P.F. Xia, Y. Li, W.K. Ho, J.G. Yu, Appl. Surf. Sci. 391 (2017) 175–183.
- [65] J.L. Lv, K. Dai, J.F. Zhang, L. Geng, C.H. Liang, Q.C. Liu, G.P. Zhu, C. Chen, Appl. Surf. Sci. 358 (2015) 377–384.
- [66] J.Q. Yan, H. Wu, H. Chen, Y.X. Zhang, F.X. Zhang, S.Z. Frank Liu, Appl. Catal. B: Environ. 191 (2016) 130–137.
- [67] Y.Z. Hong, Y.H. Jiang, C.S. Li, W.Q. Fan, X. Yan, M. Yan, W.D. Shi, Appl. Catal. B: Environ. 180 (2016) 663–673.